

Reversible and irreversible processes during cyclic voltammetry of an electrodeposited manganese oxide as catalyst for the oxygen evolution reaction

Javier Villalobos¹, Ronny Golnak², Lifei Xi¹, Götz Schuck³ and Marcel Risch^{1,4,*}

¹ Nachwuchsgruppe Gestaltung des Sauerstoffentwicklungsmechanismus, Helmholtz-Zentrum Berlin für Materialien und Energie GmbH, Hahn-Meitner Platz 1, 14109 Berlin, Germany

² Department of Highly Sensitive X-ray Spectroscopy, Helmholtz-Zentrum Berlin für Materialien und Energie, Albert-Einstein-Straße 15, 12489 Berlin, Germany

³ Department of Structure and Dynamics of Energy Materials, Helmholtz-Zentrum Berlin für Materialien und Energie, Hahn-Meitner Platz 1, 14109 Berlin, Germany

⁴ Institut für Materialphysik, Georg-August-Universität Göttingen, Friedrich-Hund-Platz 1, 37077 Göttingen, Germany

* marcel.risch@helmholtz-berlin.de

Abstract

Manganese oxides have received much attention over the years among the wide range of electrocatalysts for the oxygen evolution reaction (OER) due to their low toxicity, high abundance and rich redox chemistry. While many previous studies focused on the activity of these materials, a better understanding of the material transformations relating to activation or degradation is highly desirable, both from a scientific perspective and for applications. We electrodeposited Na-containing MnO_x without long-range order from an alkaline solution to investigate these aspects by cyclic voltammetry (CV), scanning electron microscopy (SEM) and X-ray absorption spectroscopy (XAS) at the Mn-K and Mn-L edges. The pristine film was assigned to a layered edge-sharing Mn^{3+/4+} oxide with Mn-O bond lengths of mainly 1.87 Å and some at 2.30 Å as well as Mn-Mn bond lengths of 2.87 Å based on fits to the extended X-ray fine structure (EXAFS). The decrease of the currents at voltages before the onset of the OER followed power laws with three different exponents depending on the number of cycles and the Tafel slope decreases from 186±48 to 114±18 mV dec⁻¹ after 100 cycles, which we interpret in the context of surface coverage with unreacted intermediates. Post-mortem microscopy and bulk spectroscopy at the Mn-K edge showed no change of the microstructure, bulk local structure or bulk Mn valence. Yet, the surface region of MnO_x oxidized toward Mn⁴⁺, which explains the reduction of the currents in agreement with literature. Surprisingly, we find that MnO_x reactivates after 30 minutes at open-circuit (OC), where the currents and also the Tafel slope increase. Reactivation processes during OC are crucial because OC is unavoidable when coupling the electrocatalysts to intermittent power sources such as solar energy for sustainable energy production.

Introduction

Among the wide range of transition metal oxides used for the oxygen evolution reaction (OER), manganese oxides have received much attention over the years because their low toxicity and their high abundance (10th in Earth crust). Furthermore, photosystem II has an active site consisting of CaMn₄O₅, which makes manganese oxides scientifically interesting as biomimetic catalysts [1–6]. In the past years, the attention was mainly focused on simple manganese oxides [3–13], such as Mn₃O₄, Mn₂O₃, MnO₂ and variants with non-binding, redox-inactive cations, e.g. δ-AMnO₂ (A is group I/II cation) [14–16]. The activation and degradation processes of Mn oxides are less understood than the activity of these catalysts. Usually, degradation is associated with changes of the surface and bulk oxide composition, long range order (i.e. crystallinity) and/or microstructure, but it can be also caused by detachment, particle agglomeration, or blocking by oxygen bubbles [17–21]. These material modifications due to activation and degradation can be electrochemically observed as changes in overpotential at fixed current or changes in current at fixed overpotential [17,22–24]. Cyclic voltammetry (CV) is the other common electrochemical test of these processes and frequently used as an activation procedure [25–28]. This activation procedure is also known as pretreatment or conditioning, and it is usually carried out as several cycles in a limited range of voltage. The promotion of the catalytic properties after an activation process has been studied for oxides such as Ir- [26,28], Co- [27,29] and also Mn-based oxides [25,30]. Common sweep speeds for these studies are in the range of 10 to 200 mV/s, while they are slower for studies with the focus on activity. Typically, the activation is performed for 20 to 50 cycles, but in some cases, the final activated material does not form until the 200th cycle [31].

Understanding the processes of activation and degradation of oxides in alkaline media requires measurements complementary to electrochemical methods. Frydendal et al. [32] argue that the stability degradation of electrodeposited Mn oxides cannot be determined based on electrochemical experiments alone, which is supported by gravimetric experiments using an electrochemical quartz crystal microbalance (EQCM) and inductively coupled plasma mass spectrometry (ICP-MS). Geiger et al. [33] recently proposed the S-number as a metric of catalyst degradation which requires the determination of the material loss, e.g. by ICP-MS measurements. Köhler et al. [1] and Baumung et al. [34] studied the activation of LiMn₂O₄ particles during CV using a rotating ring-disk electrode (RRDE) where the ring was set to a voltage sensitive to dissolved Mn.

Valuable insight into the mechanism of catalysis, activation and degradation of manganese oxides has been obtained in the last decade from spectroscopy including X-ray absorption spectroscopy (XAS) [35–43], UV-Vis spectroscopy [44–46] and Raman spectroscopy [46]. We focus on alkaline electrolytes herein. The distinction between acidic, neutral and alkaline conditions is important because Mn³⁺ ions disproportionate to Mn²⁺ and Mn⁴⁺ in acidic and neutral electrolytes, while Mn²⁺ and Mn⁴⁺ ions comproportionate to Mn³⁺ in alkaline electrolytes [44,45]. Nakamura and coworkers [44,45] discuss that more Mn³⁺ ions lead to higher activity, which is in line with the e_g orbital descriptor proposed by Suntivich et al.[47]. In their catalytic model, comproportionation of Mn⁴⁺ serves as a secondary supply of the catalytically active Mn³⁺, which may explain that the lowest overpotential in systematic studies of the OER on simple manganese oxides is usually found for mixed Mn^{3+/4+} oxides [3,4,38–40,42]. Therefore, it is critical to control the distribution of Mn cations in Mn-based electrocatalysts for the OER to understand their activity and potential degradation. Jaramillo and coworkers showed precious support materials (e.g. Au) induce Mn oxidation after the OER to such a mixed Mn^{3+/4+} oxide [41,43]. Moreover, the voltage range in CV can have drastic influence on the observed redox features and thus the nature of the Mn oxide

[46,48]. Post-mortem and in situ experiments on many Mn oxides show clear valence changes during electrocatalytic experiments in alkaline media [37–40], often accompanied by structural changes [35,36]. Interestingly, studies including low voltages in addition to those supporting the OER often show the formation of Mn_3O_4 ($\text{Mn}^{2+}\text{Mn}^{3+}_2\text{O}_4$), which was not present in the pristine material [35,38,46]. The exact role of tetrahedral Mn^{2+} in Mn_3O_4 is unknown but Rabe et al. [46] show that it hinders Mn dissolution using a combination of in situ Raman spectroscopy and ICP-MS.

In this study, we electrodeposited Na-containing MnO_x films without long-rang order directly in an alkaline electrolyte using a complexing agent, while most other manganese oxide catalysts are deposited at lower pH (e.g. [12]). By this approach, we avoid complications due to ion exchange and focus on the changes of the Mn valence to identify activation and degradation processes during cyclic voltammetry and open-circuit conditions at pH 13. Electrochemical changes were observed and correlated with post-mortem XAS. Unexpectedly, we found that our MnO_x films reactivate after open-circuit.

Methods

Materials

$\text{Mn}(\text{NO}_3)_2 \cdot 4\text{H}_2\text{O}$ ($\geq 99.99\%$), MnO_2 ($\geq 99\%$), Mn_3O_4 ($\geq 97\%$), Mn_2O_3 ($\geq 99.9\%$), L-(+)-Tartaric acid ($\geq 99.5\%$) and (2 M and 0.1 M) NaOH solutions were ordered from Sigma-Aldrich. Graphite foil (≥ 99.8) with a thickness of 0.254 mm ordered from VWR, deionized water ($>18\text{ M}\Omega\text{ cm}$). All reactants were used as received, without any further treatment.

Electrodeposition of MnO_x films

0.6 mmol of $\text{Mn}(\text{NO}_3)_2 \cdot 4\text{H}_2\text{O}$ and 6 mmol of L-(+)-tartaric acid were dissolved in a small volume of deionized water (approx. 1 mL). 120 mL of Ar-purged 2 M NaOH solution were added slowly with stirring to the previous solution, changing from colorless to beige.

Electrodeposition was carried out using a Gamry 600+ potentiostat and a three-electrode cell made from a three-neck round-bottom flask. The separation between the necks and thus electrodes was less than 1 cm. The working electrodes were either a glassy carbon disk (4 mm diameter; HTW Sigradur G) in a rotating disk electrode (RDE) or graphite paper (Alfa Aesar). The unrotated RDE was mounted onto a commercial rotator (ALS RRDE-3A Ver 2.0). We used a saturated calomel reference electrode (SCE; ALS RE-2BP) and a graphite rod (redox.me, HP-III, High Pure Graphite) as the counter electrode. The galvanostatic deposition was performed at $150\ \mu\text{A}/\text{cm}^2$ until a charge density of $40\ \text{mC}/\text{cm}^2$ was reached.

Electrochemical measurements

The detailed protocol for electrocatalytic investigations is documented in Table S1 for glassy carbon electrodes and in Table S2 for graphite foil. The measurements on glassy carbon electrodes were carried out using two Gamry 600+ potentiostats connected as a bipotentiostat in a single-compartment three-electrode electrochemical cell made of polymethyl pentene (ALS) filled with about 60 mL solution of 0.1 M NaOH (pH 13). A commercial rotator (ALS RRDE3-A Ver 2.0) was used with commercial rotating ring-disk electrodes with exchangeable disks of 4 mm diameter and a Pt ring with inner ring diameter of 5 mm and outer diameter of 7 mm. The graphite foil was clamped in the same cell as the RRDE. A coiled platinum wire was used as a counter electrode and a SCE (ALS RE-2BP) as a reference electrode, which was

calibrated daily against a commercial reversible hydrogen electrode (RHE; Gaskatel HydroFlex) as detailed in Fig. S1. The electrochemical experiments were performed at constant controlled temperature of 25.0 °C. The ring was set to detect oxygen at 0.4 V vs. RHE as calibrated previously [34]. Before any experiment, the electrolyte was purged with Ar for at least 30 minutes. Typical electrolyte resistances of $R = 40 \pm 9 \Omega$ were determined by electrochemical impedance spectroscopy (EIS) (representative data in Fig. S2a). The ohmic drop (also called iR drop) was corrected during post-processing by subtraction of iR from the measured voltages, where i and R are the measured current and resistance (Fig. S2b). All voltages are given relative to the reversible hydrogen electrode (RHE).

The instantaneous Tafel slope was calculated by the first derivative of the iR -corrected voltage as function of the logarithm of the current density. The Tafel slope was also calculated with a fitting of voltage as function of the logarithm of the current, using the cathodic half-cycle of the cyclic voltammetry of iR -corrected data in the range between 1.71 and 1.77 V vs. RHE. The electrodes were swept at 100 mV s^{-1} and rotated at 1600 rpm. The Tafel slope was obtained by linear regression of the iR -corrected voltage ($E - iR$) against $\log_{10}(i)$. The error represents the standard deviation of three independently prepared electrodes.

Scanning electron microscopy (SEM) and energy dispersive X-ray spectroscopy (EDX)

The sample morphology was determined using a Zeiss LEO Gemini 1530 scanning electron microscope, acceleration voltage of 3 keV and in high vacuum (around 10^{-9} bar) and using a secondary electron inLens detector. The images were taken in different regions of the sample to get representative data. EDX measurements were performed using a Thermo Fischer detector with an acceleration voltage of 12 keV.

X-ray absorption spectroscopy (XAS)

All XAS data were collected at an average nominal ring current of 300 mA in top-up and multi-bunch mode at the BESSY II synchrotron operated by Helmholtz-Zentrum Berlin.

Soft XAS measurements at the Mn-L edges were conducted using the LiXEdrom experimental station at the UE56/2 PGM-2 beamline [49]. Reference samples were measured as finely dispersed powders attached to carbon tape and electrodeposited samples were measured on graphite foil (Alfa Aesar). All samples were measured at room temperature and in total electron yield (TEY) mode and with horizontally linear polarization of the beam. The TEY measurements were carried out by collecting the drain current from the sample. The sample holder was connected to an ammeter (Keithley 6514). In order to avoid radiation damage, the incoming photon flux was adjusted to get a TEY current from the sample of around 10 pA. In addition, the sample was kept as thin as possible. XAS spectra for each sample were collected at a few locations to ensure representativity of the data and further minimize radiation damage and local heating. The energy axis was calibrated using a Mn-L edge spectrum of MnSO_4 as a standard where the maximum of the L_3 -edge was calibrated to 641 eV (Fig. S3). This reference was calibrated against molecular oxygen as described elsewhere [38,50]. All spectra were normalized by the subtraction of a straight line obtained by fitting the data before the L_3 edge and division by a polynomial function obtained by fitting the data after the L_2 edge (Fig. S4).

Hard XAS at Mn-K edge was performed at the KMC-2 beamline [51]. The general used setup was organized as it follows: I_0 ionization chamber, sample, I_1 ionization chamber or FY detector, energy reference and I_2 ionization chamber. The used double monochromator consisted of two Ge-graded Si(111) crystal

substrates[52] and the polarization of the beam was linear horizontal. Reference samples were prepared by dispersing a thin and homogenous layer of the powder on Kapton tape, after removing excess of powder, the tape was folded several times to get 2 cm x 1 cm windows. Reference samples were measured in transmission mode between two ion chambers detector at room temperature. Electrodeposited samples were measured on graphite foil in fluorescence mode with a Bruker X-Flash 6/60 detector. Energy calibration of the X-ray near edge structure (XANES) was made with the corresponding metal foil, setting the inflection point for Mn at 6539 eV. All spectra were normalized by the subtraction of a straight line obtained by fitting the data before the K edge and division by a polynomial function obtained by fitting the data after the K edge (Fig. S5). The Fourier transform (FT) of the extended X-ray absorption fine structure (EXAFS) was calculated between 40 and 440 eV (3.2 to 10.7 Å⁻¹) above the Mn-K edge (E₀ = 6539 eV). A cosine window covering 10% on the left side and 10% on the right side of the EXAFS spectra was used to suppress the side lobes in the FTs.

EXAFS simulations were performed using the software SimXLite. After calculation of the phase functions with the FEFF8-Lite [53] program (version 8.5.3, self-consistent field option activated). Atomic coordinates of the FEFF input files were generated from the structure of MnOOH·xH₂O (birnessite) [54]; the EXAFS phase functions did not depend strongly on the details of the used model. An amplitude reduction factor (S⁰²) of 0.7 was used. The data range used in the simulation was 44 to 420 eV (3.4 to 10.5 Å⁻¹) above the Mn-K edge (E₀ = 6539 eV). The EXAFS simulations were optimized by the minimization of the error sum obtained by summation of the squared deviations between measured and simulated values (least-squares fit). The fit was performed using the Levenberg–Marquardt method with numerical derivatives.

Results and Discussion

Electrodeposition of films on glassy carbon

An electrodeposition protocol was developed to produce Mn oxides at alkaline pH. In these electrolytes, manganese might deposit in a numerous of stable oxide forms, commonly Mn₃O₄ (Mn⁺², Mn⁺³), Mn₂O₃ (Mn⁺³) or MnO₂(Mn⁺⁴) [55]. Conventionally, solvated Mn²⁺ cations would spontaneously precipitate as oxides or hydroxides at pH > 8. Therefore, we stabilized them using tartrate as a complexing agent to control their deposition in NaOH (inset of Fig. 1a). Furthermore, electrolyte anions may exchange with the deposited films, e.g. [31], which is prevented when the electrolyte composition does not change significantly during deposition and catalytic investigation.

Manganese oxides were deposited on glassy carbon electrodes for electrocatalytic investigations and on graphite paper for X-ray absorption spectroscopy (XAS). We first focus on the discussion of the samples deposited on glassy carbon disks. The deposition setup consisted of a commercial rotator for RDEs and a three-electrode cell (Fig S6). The films were deposited at constant current density of 150 μA/cm² (Fig. 1a), which allows to control the deposited charge by stopping the experiment after a certain time. The deposition profiles of MnO_x showed increasing voltage after short times and reached a steady-state after about 20 s. The steady -state voltage of the samples was 1.66 ±0.04 V vs. RHE and the final deposited charge density after 34 s was 40 mC/cm².

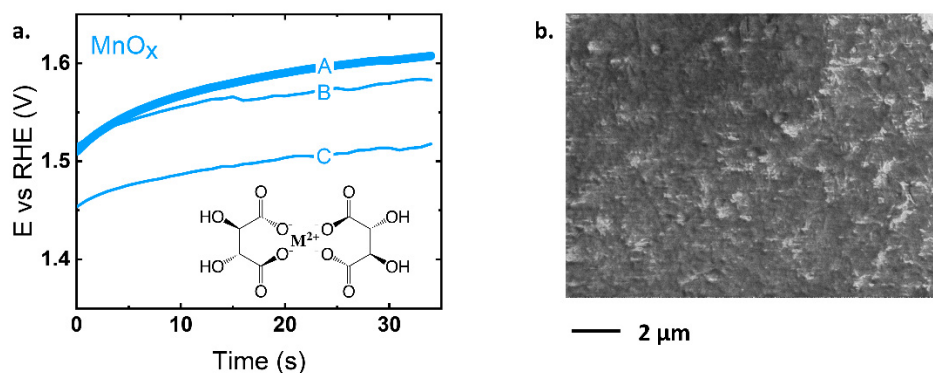


Figure 1. a. Chronoamperometry during electrodeposition of MnO_x films on glassy carbon, samples A (thick line), B and C (thin lines). The inset shows the coordination complex of divalent metal (M^{2+}) due to the presence of tartrate ions. **b.** SEM image of sample A.

The film corresponding to MnO_x sample A in Fig. 1a was subsequently characterized by SEM and EDX to check the coverage and homogeneity of the film. As it can be seen in Fig. 1b, MnO_x covered the whole surface of the glassy carbon substrate with texture on the micrometer scale. EDX elemental mapping showed a homogeneous distribution of the electrodeposited Mn and O atoms (Fig. S8), thus corroborating the formation of MnO_x anywhere on the substrate. Our films also contained Na (Fig. S8b), likely between layers of MnO_x . The crystallinity of the film was too low to be resolved by X-ray diffraction (XRD). In summary, the developed alkaline electrodeposition protocol ensured producing homogeneously covered films of Na-containing MnO_x without long-range order.

Electrocatalytic investigations

In order to evaluate the catalytic activity, activation and possible degradation of the films on glassy carbon disks, series of CV were performed in a RRDE station (representative data of MnO_x sample A in Fig. 2 and all data in Fig. S7). The sweep speed was 100 mV s^{-1} , which is typical for activation studies, while cycling is a typical method for activation studies [30,56–58]. The CVs of the MnO_x disks show an exponential increase of the current density at about 1.65 V vs. RHE for the 2nd cycle and 1.70 V vs. RHE for the 100th cycle. Additionally, about half the maximum current density was lost during 100 cycles. There were no additional redox peaks in the CV. The MnO_x film disks showed hysteresis, i.e. capacitive currents, which reduced with cycling (insets of Fig. 2). Furthermore, the current offset reduced with cycling. The offset could be eliminated by selecting a wider scan range to more negative voltages (Fig. S9). The presence of the shifts in Fig. 2 may thus indicate an incomplete reduction process that is continued over many cycles.

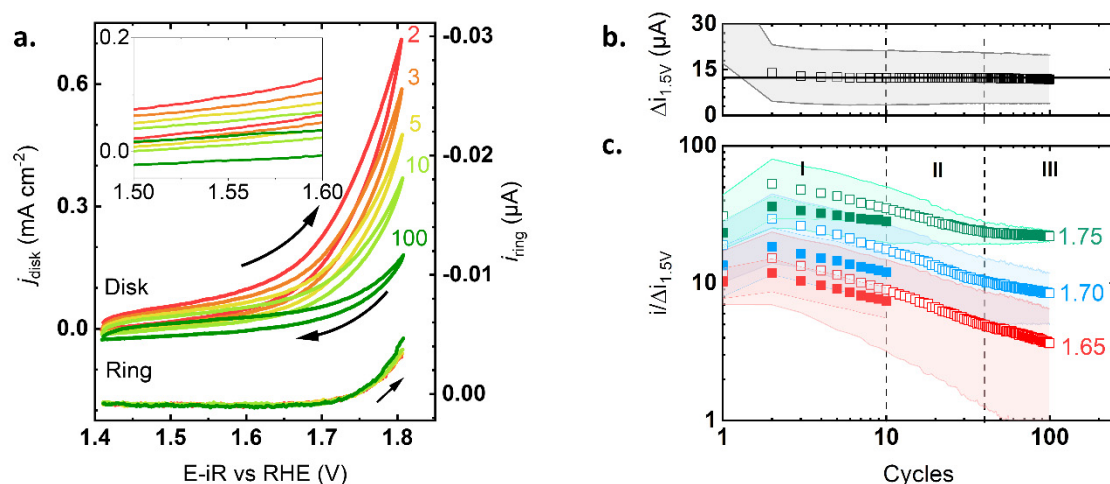


Figure 2. **a.** CV performed on a MnO_x -covered disk (sample A) with a scan rate of 100 mV s^{-1} in 0.1 M NaOH with rotation 1600 rpm and constant voltage of 0.4 V vs. RHE at the ring. **b.** Average $\Delta i_{1.5\text{V}}$ of all samples as function of cycles for the first 100 cycles (calculation detailed in the text). **c.** Average current ratio $i/\Delta i_{1.5\text{V}}$ of all samples as function of cycling at selected voltages. The data was evaluated during the first 100 cycles (open squares) and 10 cycles after 30 minutes of OCV (solid squares). The dashed lines delimit three different regions, labeled as I, II and III.

The onset of the OER was determined using the anodic ring currents, which we assign to oxygen detection by reduction [34]. The cathodic ring scan is not shown as it shows hysteresis due to delayed oxygen release. The traces of the anodic ring currents were more similar than those of the disk currents. The onset of the OER on MnO_x was consistently at 1.70 V vs. RHE independent of the cycle number as determined by the rise of the currents above the noise level. The differences in the trends between the disk and ring currents suggest that MnO_x changes electrochemically with cycling without affecting the oxygen detected at the ring.

The trends of the disk currents during cycling were also evaluated at selected voltages with and without oxygen evolution (Fig. 2b,c). The currents were corrected for capacitance by averaging the anodic and cathodic scans [59]. To account for differences in surface area for the different films with the same composition, all currents were divided by the difference between the anodic and cathodic currents at 1.50 V vs. RHE ($\Delta i_{1.5\text{V}}$). After 5 cycles, $\Delta i_{1.5\text{V}}$ becomes steady with average values of $12 \pm 1 \text{ } \mu\text{A}$ (Fig. 2b). The differential capacity is defined as $C = dQ/dE \approx \Delta i / (\Delta E / \Delta t)$ where $\Delta E / \Delta t$ is the sweep speed (here: 100 mV s^{-1}). This is a rough approximation as the capacitance is commonly obtained by systematic experiments at several sweep speeds [60]. Yet, it allows tracking the changes of surface area with cycling using the regular CV method. SEM showed no significant morphology changes after 100 cycles for the three MnO_x samples (Fig. S10).

The current ratios $i/\Delta i_{1.5\text{V}}$ of MnO_x followed a power law with different exponents depending number of cycles and whether oxygen is evolved (Fig. 2c; open symbols). A large negative exponent means fast decay of the current with cycle number, while a large positive exponent means a fast increase of the currents with cycling. The exponent was about $-1/3$ for the initial 10 cycles (region I), about $-1/4$ for intermediate

cycles (10 to 40; region II) and depended on the applied voltage for the later cycles, i.e. after about 40 cycles (region III). The exponent was similar to the initial value of $-1/3$ before the onset of the OER (1.65 V vs. RHE); it was about $-1/5$ at the onset (1.70 V) and close to zero for oxygen evolution (1.75 V vs. RHE). The spread of the currents (light colored area) was smallest for the steady-state (zero exponent) at this voltage.

In summary, the currents decreased with cycling for MnO_x and reached a steady-state only at the voltage which support oxygen evolution (1.75 V vs. RHE). These trends can be explained by (1) change in coverage with intermediates (hydroxylation or O_2 coverage) [1,61], (2) material dissolution [17], modifications of the catalyst material such (3) change in structure [19] or (4) transition metal valence [18]. The transient changes of point (1) can only be investigated in situ, while the irreversible changes of points (2)-(4) are expected to persist in a post-mortem experiment. Other explanations may be possible, but we deem these points the most likely ones and thus we address these possible explanations of the trends point by point below.

To distinguish irreversible surface changes and transient changes, we let the films rest at open-circuit voltage (OCV) for 30 minutes and then performed an additional 10 cycles. This simple test was recently introduced by El-Sayed et al. [62] for galvanostatic measurements using RDEs of iridium on ATO (antimony-doped tin oxide). The authors attribute the unexpected recovery of currents after OCV to the removal of nano and micro bubbles of oxygen within the catalyst layer, i.e. a change of (product) coverage. Here, we extend it to electrocatalyst tests using CV (Fig. 2b; solid symbols).

The exponents of the current ratio differed depending on the previously applied voltage after the OCV period for all films, suggesting partially reversible processes. The exponent was identical ($-1/3$) below the onset of the OER and less negative at the onset ($-1/4$) and above ($-3/20$). Furthermore, the current ratios were offset to lower values, i.e. the prefactor of the power law was lower. We interpret these observations as follows: the reduced prefactor indicates irreversible changes due to a reduction of active sites, either by material dissolution or deactivation of the active sites. Note that we normalized by a quantity proportional to the surface area so that we can exclude it as the source of the lower prefactor and hence currents. We cannot exclude dissolution of specific cations that leads to a different surface composition as observed, e.g. for the perovskite $\text{La}_{0.6}\text{Sr}_{0.4}\text{MnO}_3$ [63]. We attribute the changes in the exponent to a combination of transient changes of species adsorbed on the surface and the irreversible changes listed above.

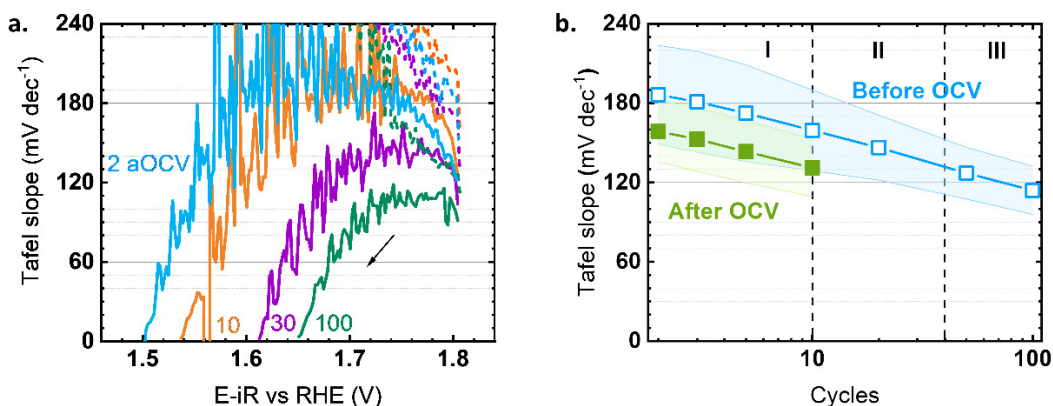


Figure 3. a. Instantaneous Tafel slope as function of voltage of cycles 10, 30 and 100 before OCV and cycle 2 after OCV (2aOCV). All Tafel slope values were calculated from CVs with a scan rate of 100 mV s^{-1} in 0.1 M NaOH rotated at 1600 rpm . Arrows show the direction of the scan. **b.** Averaged Tafel slope as function of cycle before (open symbols) and after (solid symbols) OCV. The light-colored areas represent the standard deviation of three samples. The Tafel slopes were calculated between $1.73 \text{ V} - 1.78 \text{ V}$ vs. RHE.

The Tafel slope ($b = \partial \log i / \partial E$) in chemical equilibrium depends on the surface coverage where usually limiting cases of the adsorption isotherms are discussed [1,61,64,65]. Since these values do not depend on the amount of compound or active sites, they are usually associated with mechanisms of specific reactions and vast reported values can be found for a wide range of materials in OER catalysis. The Tafel slope is very large (approaching infinity) if an early chemical step limits the reaction without any pre-equilibria [61]. In particular, very large Tafel slopes are also expected if the intermediate that reacts chemically during the rate-limiting step approaches full surface coverage in the Langmuir adsorption model [61]. A Tafel slope of 120 mV dec^{-1} is predicted (at $25 \text{ }^\circ\text{C}$) if an electrochemical step limits the kinetics, if the electrochemically reacting intermediate reaches full coverage in the Langmuir model or if the chemically reacting intermediate reaches full coverage in the Temkin model [61]. A Tafel slope of 60 mV dec^{-1} (at $25 \text{ }^\circ\text{C}$) indicates a chemical rate-limiting step with an electrochemical pre-equilibrium for low coverage of the reacting intermediate (in the Langmuir model) [1,61]. Values between 60 and 120 mV dec^{-1} are not predicted by common kinetic models. Thus, the Tafel slope does depend on the surface coverage but not uniquely.

We analyzed the Tafel slope during selected cycles of a representative sample (Fig. 3, all samples in Fig. S11). The Tafel slopes during the anodic scans in Fig. 3a were larger as compared to those of the cathodic scans. Clearly a sweep speed of 100 mV s^{-1} was too fast to establish a chemical equilibrium. If an electrochemical equilibrium plays a mechanistic role, then the produced intermediates were biased toward the oxidative site of the equilibrium (e.g. $\text{M}^{\text{III}}\text{OH} \rightarrow \text{M}^{\text{IV}}\text{O}$) during the cathodic scan, due to the voltages above the equilibrium voltage. During the 10th scan, the Tafel slope of MnO_x was 180 mV dec^{-1} at the onset of the OER and below it (1.7 to 1.6 V vs. RHE). Note that previously electrochemically produced intermediates can react chemically below the onset of the OER (as determined by the ring during the anodic scan). After 100 cycles, the Tafel slope decreased to 110 mV dec^{-1} between 1.8 and 1.7 V vs. RHE. In fact, the Tafel slopes decreased exponentially before and after the OCV (Fig. 3b and S12). After the OCV (2aOCV), the trace of the Tafel slope and its constant value of 180 mV dec^{-1} matched that of the 10th cycle before the OCV (Fig. 3a). In summary, the region of constant Tafel slope (or minimum) shifted to lower voltages with cycling for both materials. The Tafel slope decreased for MnO_x with cycling. After OCV, the voltage dependence and value (within error) of the Tafel slope matched those observed initially. We interpret these trends as a reversible formation of an active state (with certain intermediate coverage) on MnO_x .

Local structure and valence changes due to cycling

We used XAS to study the irreversible changes due to cycling. XAS experiments were necessary due to its fine chemical sensitivity and the absence of crystallinity required for diffraction techniques. Changes in the local structure of the oxides were identified using the EXAFS at the Mn-K edge [66–68]. The XANES

was used to discuss changes of the metal valence where we analyzed the bulk-sensitive K edge and more surface-sensitive L edge of Mn.

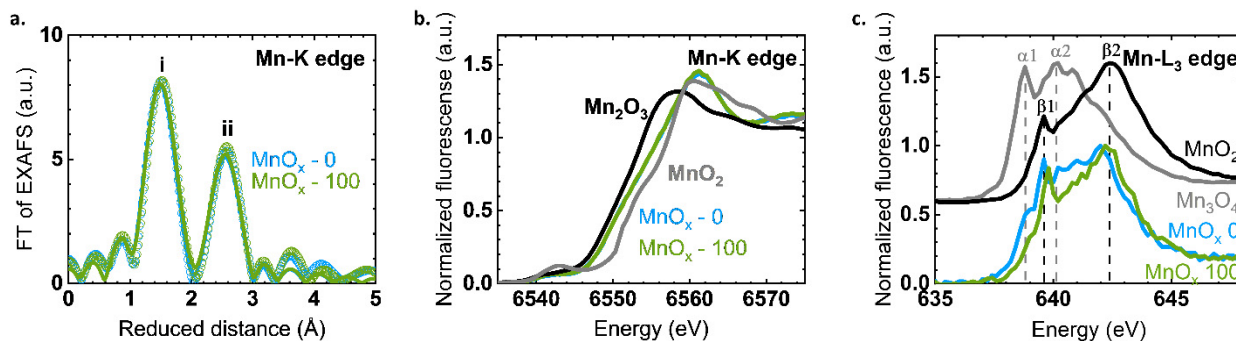


Figure 4. **a.** Fourier-transform EXAFS spectra for Mn K-edge collected on pristine MnO_x (blue symbols) and after 100 cycles of OER catalysis (green symbols). The corresponding lines are results from EXAFS simulations (see Table 1 for parameters). The reduced distance is by about 0.3 Å shorter than the precise distance obtained by EXAFS simulations. **b.** XANES spectra for Mn-K edge collected on MnO_x after 0 cycles and 100 cycles. The Mn-K edge spectra of Mn_2O_3 and MnO_2 were added as references. **c.** Mn-L₃ edge spectra for pristine MnO_x (MnO_x 0) and MnO_x after 100 cycles (MnO_x 100); and MnO_2 and Mn_3O_4 , which were used as references.

The sample for the XAS investigations were prepared on graphite foil by the same procedure as discussed above (Table S2). The deposition of the same charge density on the larger graphite foil also resulted in a steady-state after about 20 s but at lower voltages of 1.37 ± 0.03 V vs. RHE (Fig. S7). The systematic shift by about +300 mV did not affect the observed electrocatalytic behavior with cycling (Fig. S14). While there may have been minor variations of the film composition, valence and roughness due to the different steady-state voltages, the identical cycling trends strongly suggest that the trends in the XAS data can be used to rationalize the cycling trends of films deposited on both graphite foil and glassy carbon.

Table 1. EXAFS absorber–backscatter distance (R), coordination numbers (N) and Debye–Waller factor (σ) as determined by simulation of the k^3 -weighted EXAFS spectra at the Mn-K edge for pristine MnO_x . (MnO_x -0) and after 100 cycles (MnO_x -100). Shells were simulated using phase functions from a previously reported birnessite structure [54].

Sample	Parameter	Mn–O1	Mn–O2	Mn–Mn	R – factor
MnO_x -0	N	5.0	1.0	4.3	
	R (Å)	1.87	2.30	2.86	0.59 %
	σ (Å)	0.05	0.05*	0.08	
MnO_x -100	N	5.2	1.5	4.2	
	R (Å)	1.87	2.30	2.86	0.85 %
	σ (Å)	0.05	0.05*	0.08	

* indicates fixed values (not simulated).

The R-factor used Fourier filtered data between 1 and 3 Å using the formula $R_f = 100 \frac{\sum(m^{ff}-e^{ff})^2}{\sum(e^{ff})^2}$, where m^{ff} represents the Fourier-filtered model and e^{ff} represents the experimental k-weighted EXAFS curve.

The Fourier transform of the EXAFS of MnO_x showed the expected features of layered hydroxides (Fig. 4a), namely two peaks at about 1.5 and 2.5 Å reduced distance labeled i and ii, respectively. The FT of the EXAFS did not change with cycling for these peaks. We simulated peaks i and ii using $\text{MnOOH}\cdot x\text{H}_2\text{O}$ (birnessite) [54] (Fig. 4a). The fit results corroborate the assignment to a layered hydroxide as the R-factors were below 2 % [68] (Table 1). There were no drastic changes with cycling in the local structure of the bulk but we cannot exclude surface changes (additional discussion below). The metal-oxygen bond length is 1.87 Å (peak i), which is typical for $\text{Mn}^{3+/4+}\text{O}_6$ cations [54,69]. Yet, there is another Mn-O bond length of around 2.30 Å, which significantly improves the fit. This bond length is similar to the one in Mn^{2+}O and may indicate a minor impurity phase [54]. The Mn-Mn distances were 2.87 Å in MnO_x . These distances have been widely reported for amorphous electrodeposited oxides where they correspond to hexacoordinated Mn-O and di- μ -oxo bridged metals, i.e. edge-sharing octahedra [3,70]. The absence of clear FT peaks at higher reduced distance implies a lack of long-range order.

A qualitative estimation of the average bulk metal valence can be achieved by comparison of the XANES spectra of the films and suitable reference materials (Fig. 4b). The Mn-K edge spectra of MnO_x were compared with the two references $\text{Mn}^{3+}_2\text{O}_3$ and $\beta\text{-Mn}^{4+}\text{O}_2$. The edge rise of our films falls between that of the references, which indicates that the average Mn valence is between +3 and +4 in the film. The spectra of MnO_x showed negligible changes.

As catalysis is a surface process, we turned our attention to soft X-ray spectroscopy accessed by the electron yield mode. The escape depth of the electrons is 2.6 ± 0.3 nm at the Mn-L edge of a comparable oxide [71], so that we probe the near surface regions of the samples. In contrast to the K edge XANES, we found clear changes with cycling near the surface at the L_3 edge (Fig. 4c). The main peaks of the references $\text{Mn}^{2.6+}_3\text{O}_4$ and $\beta\text{-Mn}^{4+}\text{O}_2$ were labeled α_1 - α_2 and β_1 - β_2 , respectively. Peak α_1 can be assigned to Mn^{2+} in tetrahedral coordination [38]. The Mn- L_3 spectrum of pristine MnO_x was broad and contained features of both references. We found a clear reduction of the normalized spectral intensity at the energies assigned to peaks α_1 and α_2 after 100 cycles (Fig. 4b). The spectrum of MnO_x after 100 cycles closely resembled that of the MnO_2 reference but a slight shoulder at the energy of α_1 remained.

We conclude that the MnO_x films were deposited as layers of edge-sharing octahedra with low long-range order. The local bulk structure was preserved upon cycling. There were no changes in the bulk, while the surface region of MnO_x oxidizes toward Mn^{4+} and Mn_3O_4 or another phase that contained tetrahedral Mn^{2+} was consumed but did not vanish completely.

Having uncovered the local structure and surface valence changes on MnO_x , we can now interpret the trends during electrocatalytic cycling in this context. Irreversible catalyst changes lead to a decrease of the current ratio at all voltages below the onset of the OER. The current ratio at low overpotential achieved steady-state after 50 cycles, which did not persist after OCV. This irreversible decrease in current ratio could either be explained by loss of tetrahedral Mn^{2+} , possibly as Mn_3O_4 , at the surface or surface oxidation toward Mn^{4+} . While the role of the former is not well understood, there is a broad consensus on the role of Mn^{4+} as discussed in the next paragraphs.

The most commonly studied oxide with tetrahedral Mn^{2+} is Mn_3O_4 , which consists of tetrahedral Mn^{2+} and octahedral Mn^{3+} cations. Some studies state that (bulk) Mn_3O_4 is an active electrocatalyst [12,72–74], while it is the least active catalyst in comparative studies [11,25]. Thus, it is unclear if bulk Mn_3O_4 is an electrocatalyst as its electric conductivity is low [35] and other Mn oxide phases are found at the surface of bulk Mn_3O_4 such as amorphous $\text{Mn}^{3+/4+}$ -oxide [75] or birnessite-type MnO_x [11,76], both of which are formed at voltages below the onset of the OER [77,78]. Huynh et al.[79] identified Mn_3O_4 as a precursor to an active birnessite-like phase. Finally, Wei et al.[80] propose that only the octahedral Mn site is active for the OER in spinel oxides. In summary, tetrahedral Mn^{2+} is likely not directly relevant during the OER but may be important for the formation of the active phase and as a passivating phase that prevents Mn leaching [46].

The role of (octahedral) Mn^{4+} for the OER is better understood. Mn^{4+} forms at voltages below the onset of the OER [38,46]. While many of the more active Mn-based electrocatalysts contain Mn^{4+} in addition to Mn^{3+} [10,39,40,81–84], those with predominately Mn^{4+} are inactive [3]. Recently, Baumung et al. [18] showed that (bulk) oxidation of $\text{LiMn}^{3.5+}_2\text{O}_4$ toward Mn^{4+} increases the overpotential of the OER. This can be rationalized qualitatively using the occupancy of the e_g orbitals as proposed by Suntivich et al. [47] where the lowest overpotential is predicted for an e_g occupancy of about one (Mn^{3+}) and both higher or lower e_g occupancy (i.e. Mn^{2+} and Mn^{4+}) leads to an increase in overpotential. Yet, small amounts of Mn^{2+} and Mn^{4+} are beneficial if Mn comproportionation of these ions to Mn^{3+} is possible on the surface of the Mn oxide [44,45]. Thus, the lowest overpotential in systematic studies of the OER on manganese oxides is usually found between $\text{Mn}^{3.5+}$ and $\text{Mn}^{3.7+}$ [3,4,38–40,42], rather than Mn^{3+} . Nonetheless, materials with mainly Mn^{4+} perform significantly worse than those with sizable amount of Mn^{3+} , e.g. Köhlbach et al. [85] attributed the formation of Mn^{4+} on the surface to deactivation of $\alpha\text{-Mn}_2\text{O}_3$ films and Rabe et al. [46] identified the highest rate of Mn dissolution on MnO_2 during CV. Therefore, we conclude that the Mn^{4+} on the surface of our MnO_x films is responsible for the observed decrease in the current. Future studies should address the optimal amount of Mn^{4+} at the surface during the oxidizing conditions of the OER to maximize activity and to simultaneously prevent deactivation processes during catalyst conditioning or operation.

In addition to the previously reported irreversible change of manganese oxides, we also found that the film could be partially reactivated after 30 minutes at OCV (Fig. 2b and Fig. 3). The OCV was 0.97 V or lower and reached a steady-state for one sample at 0.88 V vs. RHE (Fig. S16). At these voltages, reduction of Mn^{4+} to Mn^{3+} is expected as shown by an in situ soft XAS study [38] and chemical reactions such as oxygen evolution by reduction of Mn^{4+} may occur [3]. We interpreted the increase of the measured current and of the Tafel slope as the reversible formation of an active state with a certain, still unknown, high coverage of catalytic intermediates, which could be associated with a valence change of the MnO_x surface. The elucidation of possible valence changes and thus the active state requires specialized in situ experiments which are beyond the scope of this report. We note that the identical exponents initially and after OCV suggest that Mn^{4+} is produced at the same rate after reactivation. The reactivation after OCV is significant for catalysis on manganese oxides and their activation protocol. Degradation tests based purely on electrochemical methods such as CV or voltage/current holding may suggest an irreversible material degradation while an optimized measurement protocol could recover some activity.

Conclusions

We deposited a Na-containing layered oxide of $\text{Mn}^{3+/4+}$ without long-range order in NaOH solution with a complexing agent added. The onset of the OER was at 1.7 V vs. RHE as determined by oxygen detection at the ring of an RRDE. We tracked the currents by CV during 100 cycles where 3 regions with different trends could be identified: 1-10 cycles, 10-40 cycles and 40-100 cycles. At voltages below the onset of the OER, the currents decrease with cycling but the OER currents at 1.75 V vs. RHE reached a steady-state in the 3rd region. Thus, an activation protocol at 100 mV s^{-1} should at least be performed for 40 cycles on our MnO_x . The bulk of the cycled MnO_x film was not changed but its surface was oxidized toward Mn^{4+} . It agrees with previous reports that the oxidized MnO_x surface hinders the OER. Interestingly, the currents during CV could be partially recovered after 30 minutes of OCV, which was not observed previously. We attribute the underlying process to high coverage with unreacted intermediates as supported by the high Tafel slopes. The reactivation after OCV is significant as some manganese oxides or Mn-containing oxides may be more robust as estimated based on continuous cycling. A measurement protocol without continuous cycling may prevent some but not all activity-reducing processes. Coupling of electrocatalysts to intermittent sources such as solar energy naturally leads to OCV conditions during operation. Therefore, it is important how an electrocatalyst for sustainable fuel production reacts to OCV, which is understudied.

Acknowledgements

We acknowledge Denis Antipin, Max Baumung, Florian Schönwald, Dr. Daowei Gao and Dr. Laura Pardo for helping in data collection. Frederik Stender is thanked for writing the electrochemistry analysis script and Dr. Petko Chernev for permission to use his software SimXLite. We thank Helmholtz-Zentrum Berlin (HZB) for the allocation of synchrotron radiation beamtime and acknowledge HZB CoreLab Correlative Microscopy and Spectroscopy for training and advising in SEM. This project has received funding from the European Research Council (ERC) under the European Union's Horizon 2020 research and innovation programme under grant agreement No 804092.

ORCID IDs

Javier Villalobos (0000-0002-8032-6574)

Götz Schuck (0000-0002-0624-2719)

Lifei Xi (0000-0002-5248-7936)

Marcel Risch (0000-0003-2820-7006)

Conflict of interest

The authors declare no conflict of interest.

References

- [1] Köhler L, Ebrahimizadeh Abrishami M, Roddatis V, Geppert J and Risch M 2017 Mechanistic Parameters of Electrocatalytic Water Oxidation on LiMn₂O₄ in Comparison to Natural Photosynthesis *ChemSusChem* **10** 4479–90
- [2] Najafpour M M, Heidari S, Balaghi S E, Hołyńska M, Sadr M H, Soltani B, Khatamian M, Larkum A W and Allakhverdiev S I 2017 Proposed mechanisms for water oxidation by Photosystem II and nanosized manganese oxides *Biochim. Biophys. Acta - Bioenerg.* **1858** 156–74
- [3] Zaharieva I, González-Flores D, Asfari B, Pasquini C, Mohammadi M R, Klingan K, Zizak I, Loos S, Chernev P and Dau H 2016 Water oxidation catalysis – role of redox and structural dynamics in biological photosynthesis and inorganic manganese oxides *Energy Environ. Sci.* **9** 2433–43
- [4] Melder J, Bogdanoff P, Zaharieva I, Fiechter S, Dau H and Kurz P 2020 Water-Oxidation Electrocatalysis by Manganese Oxides: Syntheses, Electrode Preparations, Electrolytes and Two Fundamental Questions *Zeitschrift für Phys. Chemie* **234** 925–78
- [5] Najafpour M M, Renger G, Hołyńska M, Moghaddam A N, Aro E-M, Carpentier R, Nishihara H, Eaton-Rye J J, Shen J-R and Allakhverdiev S I 2016 Manganese Compounds as Water-Oxidizing Catalysts: From the Natural Water-Oxidizing Complex to Nanosized Manganese Oxide Structures. *Chem. Rev.* **116** 2886–936
- [6] Wiechen M, Najafpour M M, Allakhverdiev S I and Spiccia L 2014 Water oxidation catalysis by manganese oxides: Learning from evolution *Energy Environ. Sci.* **7** 2203–12
- [7] Gao Q, Ranjan C, Pavlovic Z, Blume R and Schlögl R 2015 Enhancement of Stability and Activity of MnO_x/Au Electrocatalysts for Oxygen Evolution through Adequate Electrolyte Composition *ACS Catal.* **5** 7265–75
- [8] Kurz P 2016 Biomimetic Water-Oxidation Catalysts: Manganese Oxides. *Top. Curr. Chem.* **371** 49–72
- [9] Kumbhar V S, Lee H, Lee J and Lee K 2019 Recent advances in water-splitting electrocatalysts based on manganese oxide *Carbon Resour. Convers.* **2** 242–55
- [10] Smith P F, Deibert B J, Kaushik S, Gardner G, Hwang S, Wang H, Al-Sharab J F, Garfunkel E, Fabris L, Li J and Dismukes G C 2016 Coordination Geometry and Oxidation State Requirements of Corner Sharing MnO₆ Octahedra for Water Oxidation Catalysis: An Investigation of Manganite (γ-MnOOH) *ACS Catal.* **6** 2089–99
- [11] Ramírez A, Hillebrand P, Stellmach D, May M M, Bogdanoff P and Fiechter S 2014 Evaluation of MnO_x, Mn₂O₃, and Mn₃O₄ electrodeposited films for the oxygen evolution reaction of water *J. Phys. Chem. C* **118** 14073–81
- [12] Gorlin Y and Jaramillo T F 2010 A Bifunctional Nonprecious Metal Catalyst for Oxygen Reduction and Water Oxidation *J. Am. Chem. Soc.* **132** 13612–4
- [13] Zaharieva I, Chernev P, Risch M, Klingan K, Kohlhoff M, Fischer A and Dau H 2012 Electrosynthesis, functional, and structural characterization of a water-oxidizing manganese oxide *Energy Environ. Sci.* **5** 7081–9
- [14] Frey C E, Wiechen M and Kurz P 2014 Water-oxidation catalysis by synthetic manganese oxides-systematic variations of the calcium birnessite theme *Dalt. Trans.* **43** 4370–9

- [15] Heese-Gärtlein J, Morales D, Rabe A, Bredow T, Schuhmann W and Behrens M 2020 Factors Governing the Activity of α -MnO₂ Catalysts in the Oxygen Evolution Reaction: Conductivity vs. Exposed Surface Area of Cryptomelane *Chem. – A Eur. J.* doi: 10.1002/chem.201905090
- [16] Song L, Duan Y, Liu J and Pang H 2020 Transformation between nanosheets and nanowires structure in MnO₂ upon providing Co²⁺ ions and applications for microwave absorption *Nano Res.* **13** 95–104
- [17] Geiger S, Kasian O, Mingers A M, Nicley S S, Haenen K, Mayrhofer K J J and Cherevko S 2017 Catalyst Stability Benchmarking for the Oxygen Evolution Reaction: The Importance of Backing Electrode Material and Dissolution in Accelerated Aging Studies *ChemSusChem* **10** 4140–3
- [18] Baumung M, Kollenbach L, Xi L and Risch M 2019 Undesired Bulk Oxidation of LiMn₂O₄ Increases Overpotential of Electrocatalytic Water Oxidation in Lithium Hydroxide Electrolytes *ChemPhysChem* **20** 2981–8
- [19] Risch M, Grimaud A, May K J, Stoerzinger K A, Chen T J, Mansour A N and Shao-Horn Y 2013 Structural Changes of Cobalt-Based Perovskites upon Water Oxidation Investigated by EXAFS *J. Phys. Chem. C* **117** 8628–35
- [20] May K J, Carlton C E, Stoerzinger K A, Risch M, Suntivich J, Lee Y-L, Grimaud A and Shao-Horn Y 2012 Influence of Oxygen Evolution during Water Oxidation on the Surface of Perovskite Oxide Catalysts *J Phys Chem Lett* **3** 3264–70
- [21] Speck F D, Santori P G, Jaouen F and Cherevko S 2019 Mechanisms of Manganese Oxide Electrocatalysts Degradation during Oxygen Reduction and Oxygen Evolution Reactions *J. Phys. Chem. C* **123** 25267–77
- [22] Liu Y, Liang X, Gu L, Zhang Y, Li G D, Zou X and Chen J S 2018 Corrosion engineering towards efficient oxygen evolution electrodes with stable catalytic activity for over 6000 hours *Nat. Commun.* **9** 1–10
- [23] Lee J, Kim I and Park S 2019 Boosting Stability and Activity of Oxygen Evolution Catalyst in Acidic Medium: Bimetallic Ir–Fe Oxides on Reduced Graphene Oxide Prepared through Ultrasonic Spray Pyrolysis *ChemCatChem* **11** 2615–23
- [24] Eßmann V, Barwe S, Masa J and Schuhmann W 2016 Bipolar Electrochemistry for Concurrently Evaluating the Stability of Anode and Cathode Electrocatalysts and the Overall Cell Performance during Long-Term Water Electrolysis *Anal. Chem.* **88** 8835–40
- [25] Huynh M, Shi C, Billinge S J L and Nocera D G 2015 Nature of Activated Manganese Oxide for Oxygen Evolution *J. Am. Chem. Soc.* **137** 14887–904
- [26] Zhao S, Yu H, Maric R, Danilovic N, Capuano C B, Ayers K E and Mustain W E 2015 Calculating the Electrochemically Active Surface Area of Iridium Oxide in Operating Proton Exchange Membrane Electrolyzers *J. Electrochem. Soc.* **162** F1292–8
- [27] Xiao Q, Zhang Y, Guo X, Jing L, Yang Z, Xue Y, Yan Y M and Sun K 2014 A high-performance electrocatalyst for oxygen evolution reactions based on electrochemical post-treatment of ultrathin carbon layer coated cobalt nanoparticles *Chem. Commun.* **50** 13019–22
- [28] Oh H S, Nong H N, Reier T, Bergmann A, Gliech M, Ferreira De Araújo J, Willinger E, Schlögl R, Teschner D and Strasser P 2016 Electrochemical Catalyst-Support Effects and Their Stabilizing

- Role for IrO_x Nanoparticle Catalysts during the Oxygen Evolution Reaction *J. Am. Chem. Soc.* **138** 12552–63
- [29] Song F, Schenk K and Hu X 2016 A nanoporous oxygen evolution catalyst synthesized by selective electrochemical etching of perovskite hydroxide CoSn(OH)₆ nanocubes *Energy Environ. Sci.* **9** 473–7
- [30] Song F and Hu X 2014 Ultrathin cobalt-manganese layered double hydroxide is an efficient oxygen evolution catalyst *J. Am. Chem. Soc.* **136** 16481–4
- [31] Villalobos J, González-Flores D, Klingan K, Chernev P, Kubella P, Urcuyo R, Pasquini C, Mohammadi M R, Smith R D L, Montero M L and Dau H 2019 Structural and functional role of anions in electrochemical water oxidation probed by arsenate incorporation into cobalt-oxide materials *Phys. Chem. Chem. Phys.* **21** 12485–93
- [32] Frydendal R, Paoli E A, Knudsen B P, Wickman B, Malacrida P, Stephens I E L and Chorkendorff I 2014 Benchmarking the Stability of Oxygen Evolution Reaction Catalysts: The Importance of Monitoring Mass Losses *ChemElectroChem* **1** 2075–2081
- [33] Geiger S, Kasian O, Ledendecker M, Pizzutilo E, Mingers A M, Fu W T, Diaz-Morales O, Li Z, Oellers T, Fruchter L, Ludwig A, Mayrhofer K J J, Koper M T M and Cherevko S 2018 The stability number as a metric for electrocatalyst stability benchmarking *Nat. Catal.* **1** 508–15
- [34] Baumung M, Schönwald F, Erichsen T, Volkert C A and Risch M 2019 Influence of particle size on the apparent electrocatalytic activity of LiMn₂O₄ for oxygen evolution *Sustain. Energy Fuels* **3** 2218–26
- [35] Gorlin Y, Lassalle-Kaiser B, Benck J D, Gul S, Webb S M, Yachandra V K, Yano J and Jaramillo T F 2013 In situ X-ray absorption spectroscopy investigation of a bifunctional manganese oxide catalyst with high activity for electrochemical water oxidation and oxygen reduction. *J. Am. Chem. Soc.* **135** 8525–34
- [36] Walter C, Menezes P W, Loos S, Dau H and Driess M 2018 Facile Formation of Nanostructured Manganese Oxide Films as High-Performance Catalysts for the Oxygen Evolution Reaction *ChemSusChem* **11** 2554–61
- [37] Yang Y, Wang Y, Xiong Y, Huang X, Shen L, Huang R, Wang H, Pastore J P, Yu S-H, Xiao L, Brock J D, Zhuang L and Abruña H D 2019 In Situ X-ray Absorption Spectroscopy of a Synergistic Co–Mn Oxide Catalyst for the Oxygen Reduction Reaction *J. Am. Chem. Soc.* **141** 1463–6
- [38] Risch M, Stoerzinger K A, Han B, Regier T Z, Peak D, Sayed S Y, Wei C, Xu Z J and Shao-Horn Y 2017 Redox Processes of Manganese Oxide in Catalyzing Oxygen Evolution and Reduction: An In Situ Soft X-ray Absorption Spectroscopy Study *J. Phys. Chem. C* **121** 17682–17692
- [39] Tesch M F, Bonke S A, Jones T E, Shaker M N, Xiao J, Skorupska K, Mom R, Melder J, Kurz P, Knop-Gericke A, Schlögl R, Hocking R K and Simonov A N 2019 Evolution of Oxygen–Metal Electron Transfer and Metal Electronic States During Manganese Oxide Catalyzed Water Oxidation Revealed with In Situ Soft X-Ray Spectroscopy *Angew. Chemie* **131** 3464–70
- [40] Xi L, Schwanke C, Xiao J, Abdi F F, Zaharieva I and Lange K M 2017 In Situ L-Edge XAS Study of a Manganese Oxide Water Oxidation Catalyst *J. Phys. Chem. C* **121** 12003–9
- [41] Seitz L C, Hersbach T J P, Nordlund D and Jaramillo T F 2015 Enhancement Effect of Noble Metals

- on Manganese Oxide for the Oxygen Evolution Reaction *J. Phys. Chem. Lett.* **6** 4178–83
- [42] Lian S, Browne M P, Domínguez C, Stamatina S N, Nolan H, Duesberg G S, Lyons M E G, Fonda E and Colavita P E 2017 Template-free synthesis of mesoporous manganese oxides with catalytic activity in the oxygen evolution reaction *Sustain. Energy Fuels* **1** 780–8
- [43] Gorlin Y, Chung C-J, Benck J D, Nordlund D, Seitz L, Weng T-C, Sokaras D, Clemens B M and Jaramillo T F 2014 Understanding interactions between manganese oxide and gold that lead to enhanced activity for electrocatalytic water oxidation. *J. Am. Chem. Soc.* **136** 4920–6
- [44] Takashima T, Hashimoto K and Nakamura R 2012 Mechanisms of pH-dependent activity for water oxidation to molecular oxygen by MnO₂ electrocatalysts. *J. Am. Chem. Soc.* **134** 1519–27
- [45] Ooka H, Takashima T, Yamaguchi A, Hayashi T and Nakamura R 2017 Element strategy of oxygen evolution electrocatalysis based on: In situ spectroelectrochemistry *Chem. Commun.* **53** 7149–61
- [46] Rabe M, Toparli C, Chen Y H, Kasian O, Mayrhofer K J J and Erbe A 2019 Alkaline manganese electrochemistry studied by: In situ and operando spectroscopic methods-metal dissolution, oxide formation and oxygen evolution *Phys. Chem. Chem. Phys.* **21** 10457–69
- [47] Suntivich J, May K J, Gasteiger H A, Goodenough J B, Shao-horn Y, Calle-vallejo F, Oscar A D, Kolb M J, Koper M T M, Suntivich J, May K J, Gasteiger H A, Goodenough J B and Shao-horn Y 2011 A perovskite oxide optimized for oxygen evolution catalysis from molecular orbital principles *Science* **334** 1383–5
- [48] Köhler L, Szabadics L, Jooss C and Risch M 2019 Peroxide Yield of the (001) La_{0.6}Sr_{0.4}MnO₃ Surface as a Bifunctional Electrocatalyst for the Oxygen Reduction Reaction and Oxygen Evolution Reaction in Alkaline Media *Batter. Supercaps* **2** 364–72
- [49] Aziz E F, Xiao J, Golnak R and Tesch M 2016 LiXEdrom: High Energy Resolution RIXS Station dedicated to Liquid Investigation at BESSY II *J. large-scale Res. Facil. JLSRF* **2** 1–4
- [50] Risch M, Stoerzinger K A, Regier T Z, Peak D, Sayed S Y and Shao-Horn Y 2015 Reversibility of Ferri-/Ferrocyanide Redox during Operando Soft X-ray Spectroscopy *J. Phys. Chem. C* **119** 18903–10
- [51] Többsen D M and Zander S 2016 KMC-2: an X-ray beamline with dedicated diffraction and XAS endstations at BESSY II *J. large-scale Res. Facil. JLSRF* **2** 1–6
- [52] Erko A, Packe I, Gudat W, Abrosimov N and Firsov A 2001 A crystal monochromator based on graded SiGe crystals *Nucl. Instruments Methods Phys. Res. Sect. A Accel. Spectrometers, Detect. Assoc. Equip.* **467–468** 623–6
- [53] Ankudinov A and Ravel B 1998 Real-space multiple-scattering calculation and interpretation of x-ray-absorption near-edge structure *Phys. Rev. B - Condens. Matter Mater. Phys.* **58** 7565–76
- [54] Fontana C 1926 Struttura dell'ossido manganoso *Gazz. Chim. Ital.* **56** 396–7
- [55] Koza J A, Schroen I P, Willmering M M and Switzer J A 2014 Electrochemical synthesis and nonvolatile resistance switching of Mn₃O₄ thin films *Chem. Mater.* **26** 4425–32
- [56] Guo X, Wu F, Hao G, Peng S, Wang N, Li Q, Hu Y and Jiang W 2019 Activating hierarchically hortensia-like CoAl layered double hydroxides by alkaline etching and anion modulation strategies for the efficient oxygen evolution reaction *Dalt. Trans.* **48** 5214–21

- [57] Wang X, Tong R, Wang Y, Tao H, Zhang Z and Wang H 2016 Surface Roughening of Nickel Cobalt Phosphide Nanowire Arrays/Ni Foam for Enhanced Hydrogen Evolution Activity *ACS Appl. Mater. Interfaces* **8** 34270–9
- [58] Jiang T, Ansar S A, Yan X, Chen C, Fan X, Razmjooei F, Reisser R, Montavon G and Liao H 2019 In Situ Electrochemical Activation of a Codoped Heterogeneous System as a Highly Efficient Catalyst for the Oxygen Evolution Reaction in Alkaline Water Electrolysis *ACS Appl. Energy Mater.* **2** 8809–17
- [59] Wei C, Rao R R, Peng J, Huang B, Stephens I E L, Risch M, Xu Z J and Shao-Horn Y 2019 Recommended Practices and Benchmark Activity for Hydrogen and Oxygen Electrocatalysis in Water Splitting and Fuel Cells *Adv. Mater.* **1806296** 1–24
- [60] McCrory C C L, Jung S, Peters J C and Jaramillo T F 2013 Benchmarking Heterogeneous Electrocatalysts for the Oxygen Evolution Reaction *J. Am. Chem. Soc.* **135** 16977–87
- [61] Doyle R L, Godwin I J, Brandon M P and Lyons M E 2013 Redox and electrochemical water splitting catalytic properties of hydrated metal oxide modified electrodes *Phys Chem Chem Phys* **15** 13737–83
- [62] El-Sayed H A, Weiß A, Olbrich L F, Putro G P and Gasteiger H A 2019 OER Catalyst Stability Investigation Using RDE Technique: A Stability Measure or an Artifact? *J. Electrochem. Soc.* **166** F458–64
- [63] Scholz J, Risch M, Stoerzinger K A, Wartner G, Shao-Horn Y and Jooss C 2016 Rotating ring-disk electrode study of oxygen evolution at a perovskite surface: Correlating activity to manganese concentration *J. Phys. Chem. C* **120** 27746–56
- [64] Fletcher S 2008 Tafel slopes from first principles *J. Solid State Electrochem.* **13** 537–49
- [65] Bockris J O 1956 Kinetics of Activation Controlled Consecutive Electrochemical Reactions: Anodic Evolution of Oxygen *J. Chem. Phys.* **24** 817
- [66] Jaklevic J, Kirby J A, Klein M P, Robertson A S, Brown G S and Eisenberger P 1977 Fluorescence detection of EXAFS: Sensitivity enhancement for dilute species and thin films *Solid State Commun.* **23** 679–82
- [67] Koningsberger D C, Mojet B L, Dorssen G E Van and Ramaker D E 2000 XAFS spectroscopy ; fundamental principles and data analysis **10** 143–55
- [68] Calvin S 2013 *XAFS for Everyone* (CRC Press), doi: 10.1201/b14843
- [69] Iyer A, Del-Pilar J, King'ondou C K, Kissel E, Garces H F, Huang H, El-Sawy A M, Dutta P K and Suib. S L 2012 Water Oxidation Catalysis using Amorphous Manganese Oxides, Octahedral Molecular Sieves (OMS-2), and Octahedral Layered (OL-1) Manganese Oxide Structures *J. Phys. Chem. C* **116** 6474–83
- [70] Abrashev M V., Chernev P, Kubella P, Mohammadi M R, Pasquini C, Dau H and Zaharieva I 2019 Origin of the heat-induced improvement of catalytic activity and stability of MnOx electrocatalysts for water oxidation *J. Mater. Chem. A* **7** 17022–36
- [71] Ruosi A, Raisch C, Verna A, Werner R, Davidson B A, Fujii J, Kleiner R and Koelle D 2014 Electron sampling depth and saturation effects in perovskite films investigated by soft x-ray absorption

- spectroscopy *Phys. Rev. B - Condens. Matter Mater. Phys.* **90** 1–8
- [72] Maruthapandian V, Pandiarajan T, Saraswathy V and Muralidharan S 2016 Oxygen evolution catalytic behaviour of Ni doped Mn₃O₄ in alkaline medium *RSC Adv.* **6** 48995–9002
- [73] Guo C X, Chen S and Lu X 2014 Ethylenediamine-mediated synthesis of Mn₃O₄ nano-octahedrons and their performance as electrocatalysts for the oxygen evolution reaction *Nanoscale* **6** 10896–901
- [74] Rani B J, Ravi G, Yuvakkumar R, Hong S I, Velauthapillai D, Thambidurai M, Dang C and Saravanakumar B 2020 Neutral and alkaline chemical environment dependent synthesis of Mn₃O₄ for oxygen evolution reaction (OER) *Mater. Chem. Phys.* **247** 122864
- [75] Frey C E, Kwok F, Gonzáles-Flores D, Ohms J, Cooley K A, Dau H, Zaharieva I, Walter T N, Simchi H, Mohny S E and Kurz P 2017 Evaporated manganese films as a starting point for the preparation of thin-layer MnO: X water-oxidation anodes *Sustain. Energy Fuels* **1** 1162–70
- [76] Fekete M, Hocking R K, Chang S L Y, Italiano C, Patti A F, Arena F and Spiccia L 2013 Highly active screen-printed electrocatalysts for water oxidation based on β -manganese oxide *Energy Environ. Sci.* **6** 2222–32
- [77] Messaoudi B, Joiret S, Keddami M and Takenouti H 2001 Anodic behaviour of manganese in alkaline medium *Electrochim. Acta* **46** 2487–98
- [78] Su H-Y, Gorlin Y, Man I C, Calle-Vallejo F, Nørskov J K, Jaramillo T F and Rossmeisl J 2012 Identifying active surface phases for metal oxide electrocatalysts: a study of manganese oxide bi-functional catalysts for oxygen reduction and water oxidation catalysis. *Phys. Chem. Chem. Phys.* **14** 14010–22
- [79] Huynh M, Bediako D K and Nocera D G 2014 A Functionally Stable Manganese Oxide Oxygen Evolution Catalyst in Acid. *J. Am. Chem. Soc.* **136** 6002–10
- [80] Wei C, Feng Z, Scherer G G, Barber J, Shao-Horn Y and Xu Z J 2017 Cations in Octahedral Sites: A Descriptor for Oxygen Electrocatalysis on Transition-Metal Spinels *Adv. Mater.* **29** 1521–4095
- [81] Chan Z M, Kitchaev D A, Weker J N, Schnedermann C, Lim K, Ceder G, Tumas W, Toney M F and Nocera D G 2018 Electrochemical trapping of metastable Mn³⁺ ions for activation of MnO₂ oxygen evolution catalysts *Proc. Natl. Acad. Sci. U. S. A.* **115** E5261–8
- [82] Surendranath Y, Lutterman D A, Liu Y and Nocera D G 2012 Nucleation, growth, and repair of a cobalt-based oxygen evolving catalyst *J. Am. Chem. Soc.* **134** 6326–36
- [83] Khan M, Suljoti E, Singh A, Bonke S A, Brandenburg T, Atak K, Golnak R, Spiccia L and Aziz E F 2014 Electronic structural insights into efficient MnO_x catalysts *J. Mater. Chem. A* **2** 18199–203
- [84] Raabe S, Mierwaldt D, Ciston J, Uijtewaal M, Stein H, Hoffmann J, Zhu Y, Blöchl P and Jooss C 2012 In Situ Electrochemical Electron Microscopy Study of Oxygen Evolution Activity of Doped Manganite Perovskites *Adv. Funct. Mater.* **22** 3378–88
- [85] Kölbach M, Fiechter S, van de Krol R and Bogdanoff P 2017 Evaluation of electrodeposited α -Mn₂O₃ as a catalyst for the oxygen evolution reaction *Catal. Today* **290** 2–9

SUPPLEMENTARY MATERIAL

Reversible and irreversible processes during cyclic voltammetry of an electrodeposited manganese oxide as catalyst for the oxygen evolution reaction

Javier Villalobos¹, Ronny Golnak², Lifei Xi¹, Götz Schuck³ and Marcel Risch^{1,4,*}

¹ *Nachwuchsgruppe Gestaltung des Sauerstoffentwicklungsmechanismus, Helmholtz-Zentrum Berlin für Materialien und Energie GmbH, Hahn-Meitner Platz 1, 14109 Berlin, Germany*

² *Department of Highly Sensitive X-ray Spectroscopy, Helmholtz-Zentrum Berlin für Materialien und Energie, Albert-Einstein-Straße 15, 12489 Berlin, Germany*

³ *Department of Structure and Dynamics of Energy Materials, Helmholtz-Zentrum Berlin für Materialien und Energie, Hahn-Meitner Platz 1, 14109 Berlin, Germany*

⁴ *Institut für Materialphysik, Georg-August-Universität Göttingen, Friedrich-Hund-Platz 1, 37077 Göttingen, Germany*

Corresponding author

* marcel.risch@helmholtz-berlin.de

11 pages, 3 supplementary tables, 16 supplementary figures

Table S1. General protocol for electrochemical data collection on an RRDE station with samples on glassy carbon disks. All potentials are reported vs. RHE (pH 13).

Step	Conditions
1. Cleaning	Clean and polish electrodes, cells and any other tool properly.
2. Calibration of reference electrodes	OCV against commercial RHE electrode
3. Argon purge at OCV	At least 30 minutes
4.a. Ring EIS	Frequency: 1 MHz – 1 Hz. Points/decade: 10 OCV and take note of Ru
4.b. Disk EIS	Frequency: 1 MHz – 1 Hz. Points/decade: 10 OCV and take note of Ru
5. Disk CV: ECSA*	Hold 10 s at 1.0 V. Potential window: 0.95 V – 1.05 V. Scan rates: 50, 100, 150, 200, 250, 300, 350, 400, 450, 500 mV s ⁻¹ . Cycles: 3. Rotation: 0 rpm. Purge: Blanket. No dynamic iR compensation.
6.a. Ring conditioning	Hold ring potential for 1800 s at 0.40 V.
6.b. Ring: CA (O₂ detection)	Hold ring potential at 0.40 V.
6.c. Disk CV: OER	Potential window: 1.40 V - 1.80 V Scan rate: 100 mV/s Step size: 2 mV Cycles: 100 Rotation: 1600 rpm Purge: yes No dynamic iR compensation.
7. Disk CV: ECSA*	Hold 10 s at 1.0 V. Potential window: 0.95 V – 1.05 V. Scan rates: 50, 100, 150, 200, 250, 300, 350, 400, 450, 500 mV s ⁻¹ . Cycles: 3. Rotation: 0 rpm. Purge: Blanket. No dynamic iR compensation.
8. Disk OCV	1800 s
9.a. Disk EIS	Frequency: 1 MHz – 1 Hz. OCV and take note of Ru
9.b. Ring EIS	Frequency: 1 MHz – 1 Hz. OCV and take note of Ru
10.a. Ring conditioning	Hold ring potential for 1800 s at 0.40 V.
10.b. Ring: CA (O₂ detection)	Hold ring potential at 0.40 V.
11. Disk CV: OER	Potential window: 1.40 V - 1.80 V Scan rate: 100 mV/s Step size: 2 mV Cycles: 10 Rotation: 1600 rpm Purge: yes No dynamic iR compensation.

* not used due to inappropriate data for analysis.

Table S2. General protocol for electrochemical data collection with samples on graphite foil. All potentials are reported vs. RHE (pH 13).

1. Cleaning	Clean and polish electrodes, cells and any other tool properly.
2. Calibration of reference electrodes	OCV against commercial RHE electrode
3. Argon purge at OCV	At least 30 minutes
4. Foil CV: OER	Potential window: 1.40 V - 1.80 V Scan rate: 100 mV/s Step size: 2 mV Cycles: 100 Rotation: 1600 rpm Purge: yes No dynamic iR compensation
5. Sample rinsing	Soaked in deionized water for 5 minutes.

Table S3. Summary of the fit parameters from three sets of data used for Tafel slope calculation and their average. One example of the graphs involved in the calculation is shown in Figure S11. The average of the three values for each cycle and each sample is used to generate Figure 3b. SD represents the standard deviation of the three measurements.

Cycle	Slope \pm error (R^2)			Average \pm SD
	Sample A	Sample B	Sample C	
2	170 \pm 1 (0.999)	160 \pm 1 (0.999)	230 \pm 1 (0.999)	186 \pm 48
3	168 \pm 1 (0.999)	151 \pm 1 (0.999)	224 \pm 1 (0.999)	181 \pm 46
5	165 \pm 1 (0.999)	141 \pm 1 (0.999)	212 \pm 1 (0.999)	172 \pm 37
10	162 \pm 1 (0.999)	128 \pm 1 (0.999)	189 \pm 1 (0.999)	159 \pm 30
20	159 \pm 1 (0.999)	118 \pm 1 (0.999)	162 \pm 1 (0.999)	146 \pm 25
50	147 \pm 1 (0.999)	108 \pm 1 (0.999)	126 \pm 1 (0.999)	127 \pm 20
100	135 \pm 1 (0.999)	102 \pm 1 (0.998)	106 \pm 1 (0.999)	114 \pm 18
2aOCV*	165 \pm 1 (0.999)	133 \pm 1 (0.999)	179 \pm 1 (0.999)	159 \pm 23
10aOCV*	149 \pm 1 (0.999)	107 \pm 1 (0.999)	137 \pm 1 (0.999)	131 \pm 22

* aOCV = after OCV break.

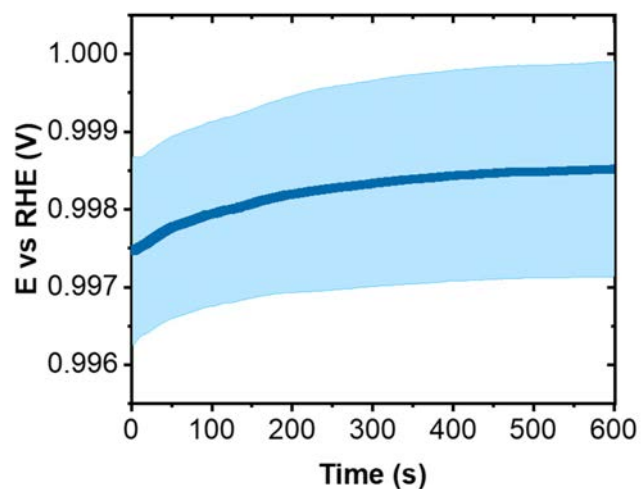


Figure S1. Calibration of reference electrode (SCE) vs. RHE. The blue line represents one single measurement and the light blue shade the error (standard deviation) of the measurements of the same two electrodes on three different days.

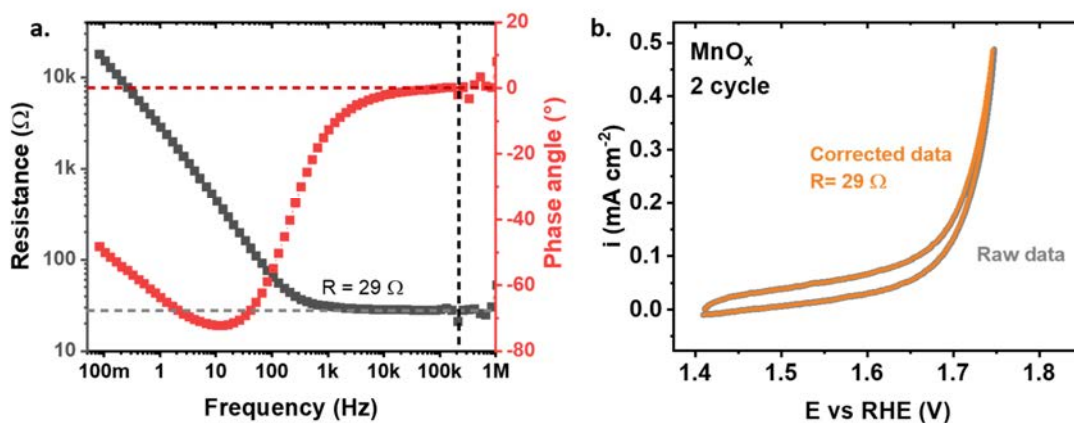


Figure S2. Example of data treatment of MnO_x after 2 cycles of catalysis: **a.** Electrochemical impedance spectrum (EIS) showing resistance (black) and phase angle (red) as function of frequency. Dashed lines represent the resistance value where the phase angle approaches zero. **b.** CV of cycle 2 with the correction of the raw data (gray) by a resistance value = 29Ω , and the resulting corrected CV (orange).

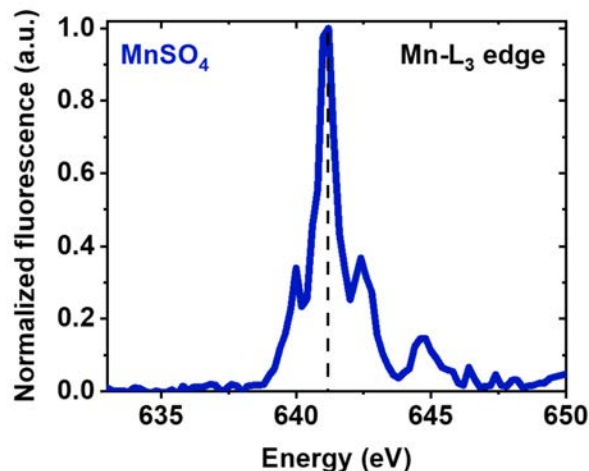


Figure S3. Mn-L₃ edge spectrum of MnSO₄, used as a reference for energy calibration. The dashed line was calibrated to 641 eV.

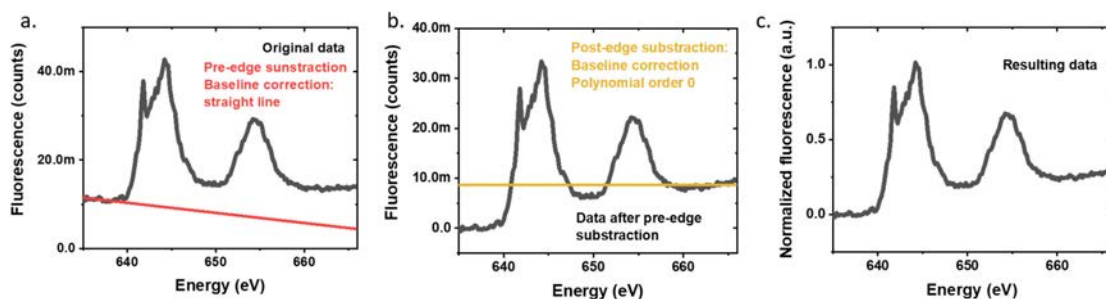


Figure S4. Spectra of a representative normalization for soft XAS of Mn-L₃ edge: **a.** Raw data (black) and baseline (red) for fitting before the edge (fit between 632 and 638 eV), **b.** Data after pre-edge subtraction (black) and baseline for fitting after the edge (yellow; fit between 660 and 667 eV), **c.** Final normalized spectrum.

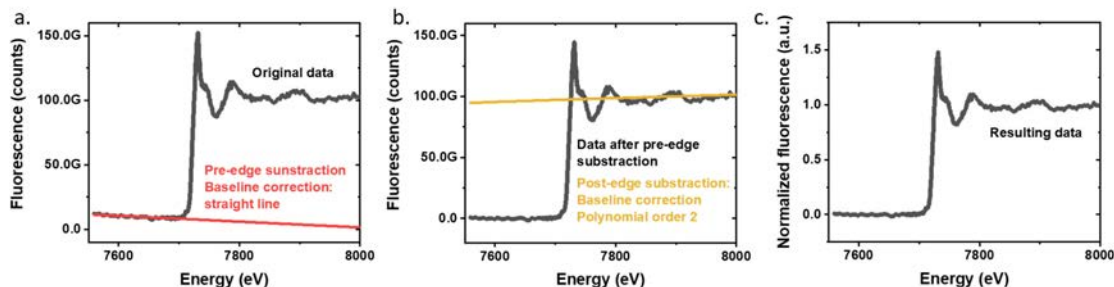


Figure S5. Spectra of a representative normalization for hard XAS of Mn-K edge (zoom on near edge region): **a.** Raw data (black) and baseline (red) for fitting before the edge (fit between 7560 and 7695 eV), **b.** Data after pre-edge subtraction (black) and fitted polynomial for division after the edge (yellow; fit between 7960 and 8255 eV) on a wider energy range as the shown spectrum, **c.** Final normalized spectrum.

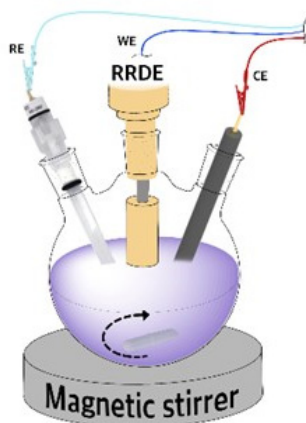


Figure S6. Scheme of the 3-electrode cell and RDE used for the electrodeposition of the films on glassy carbon.

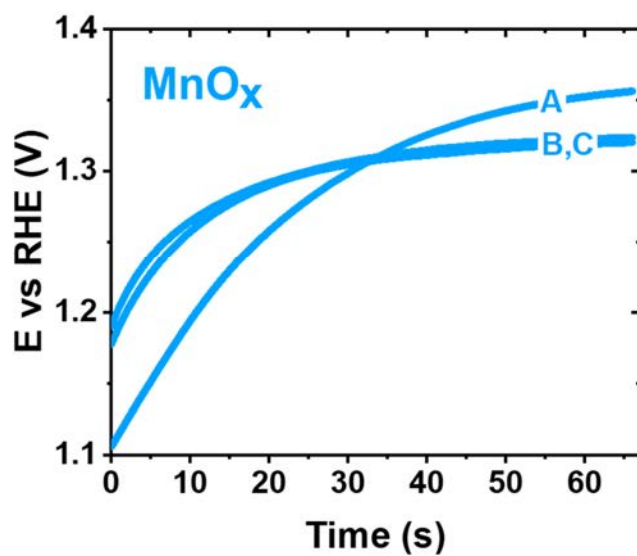


Figure S7. Chronopotentiometry during electrodeposition of MnO_x samples A, B and C on graphite foil to be characterized by XAS.

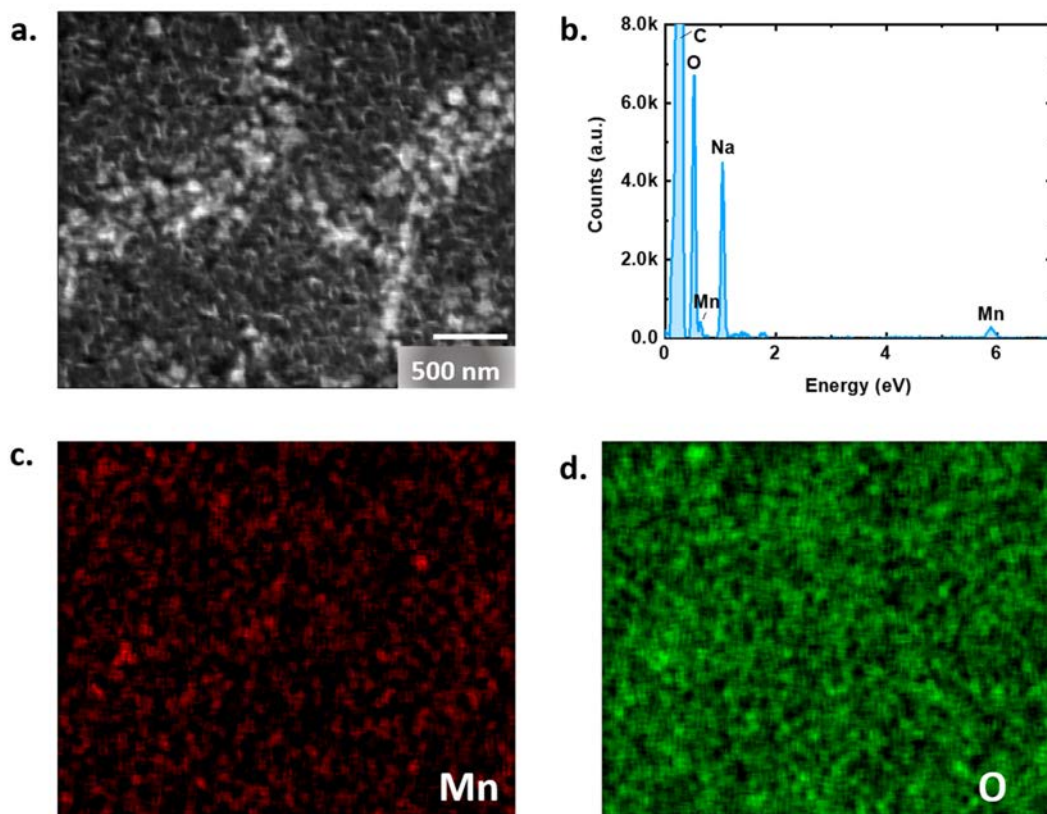


Figure S8. SEM-EDX analysis of pristine MnO_x films on glassy carbon. **a.** Gray contrast image, **b.** EDX spectrum. Elemental mapping by EDX of **c.** manganese and **d.** oxygen.

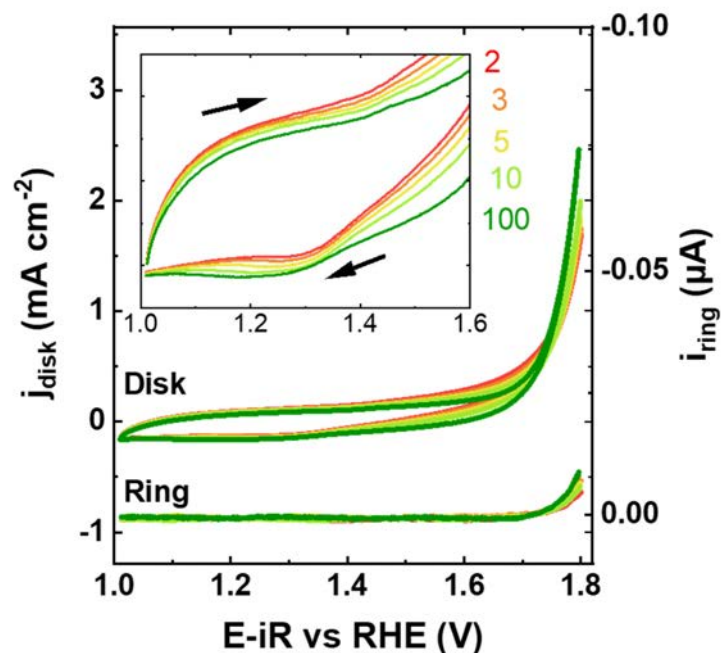


Figure S9. CV performed on a MnO_x-covered disk and step potential of 0.4 V vs. RHE at the ring. The was performed with a scan rate of 100 mV s⁻¹ in 0.1 M NaOH with rotation: 1600 rpm. This sample was measured with lower voltage boundary as samples shown in Fig. 2a. The inset shows a zoom of the region of interest due to the presence of redox peaks. The arrows indicate the direction of the scan.

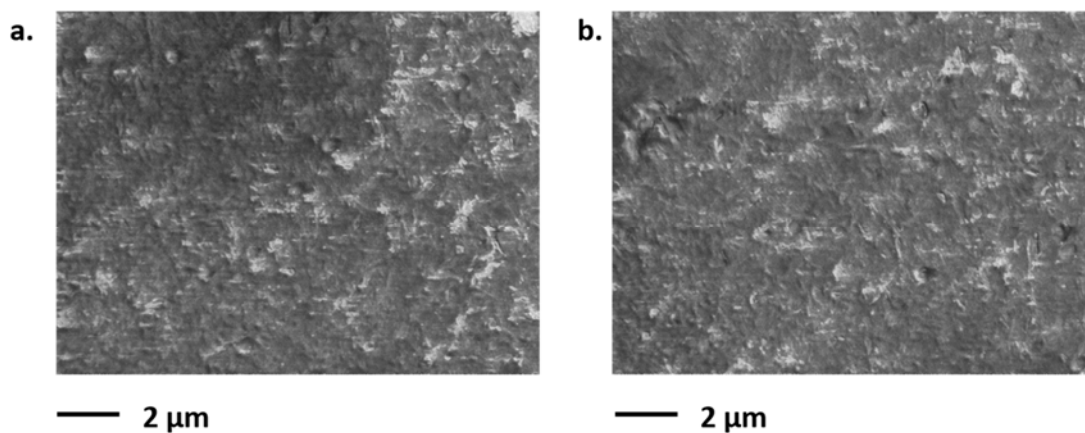


Figure S10. SEM images of: **a.** Pristine MnO_x and **b.** MnO_x after 100 cycles of OER catalysis. These measurements correspond to sample A.

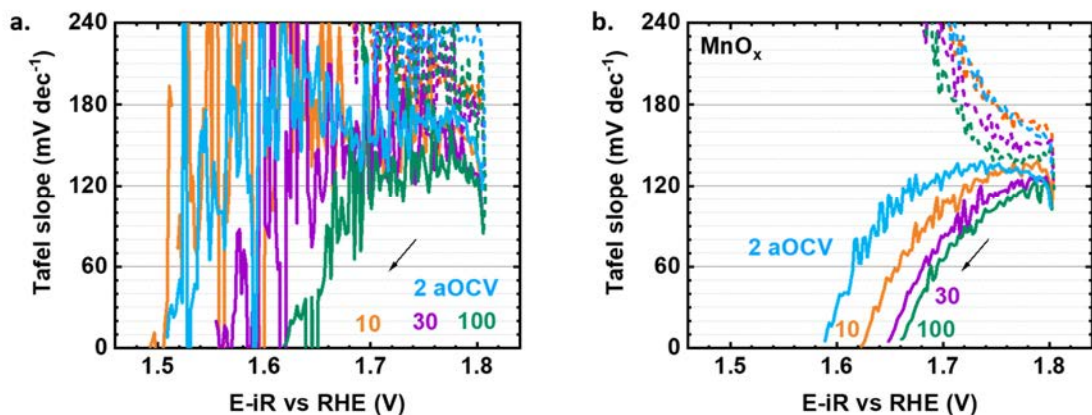


Figure S11. Instantaneous Tafel slope as function of potential of additional MnO_x films: **a.** Sample A and **b.** Sample B. Before OCV, cycles 10, 50 and 100 are shown, and after OCP cycle 2 is shown (2aOCV). All Tafel slope values were calculated from CVs with a scan rate of 100 mV s^{-1} in 0.1 M NaOH rotated at 1600 rpm . iR correction was done in post-processing. Arrows shows the direction of the CV.

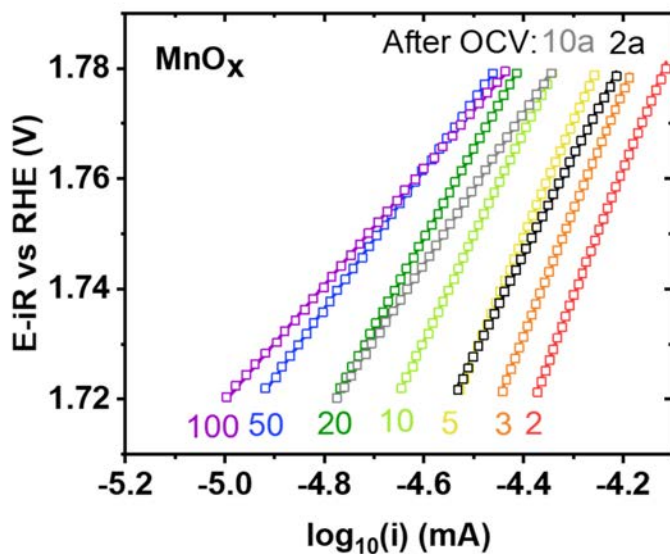


Figure S12. Representative graphs of Tafel slope calculation for selected cycles (2, 3, 5, 10, 20, 50, 100, 2 after OCV and 10 after OCV). Tafel plots of MnO_x . The measurements were performed in 0.1 M NaOH pH 13. Scan rate 100 mV s^{-1} . iR compensation was performed during post-processing. The lines represent the linear fit (denoted E-iR) of E-iR as function of $\log_{10}(i)$, the slope represents the Tafel slope. All fit parameters are summarized in Table S3.

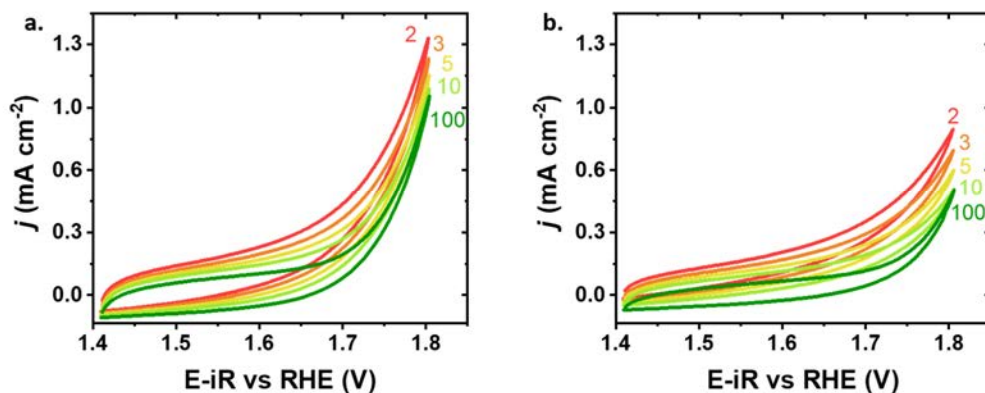


Figure S13. Series of CV of additional MnO_x films: **a.** Sample B and **b.** Sample C, performed at the disk. CV with a scan rate of 100 mV s^{-1} in 0.1 M NaOH rotated at 1600 rpm .

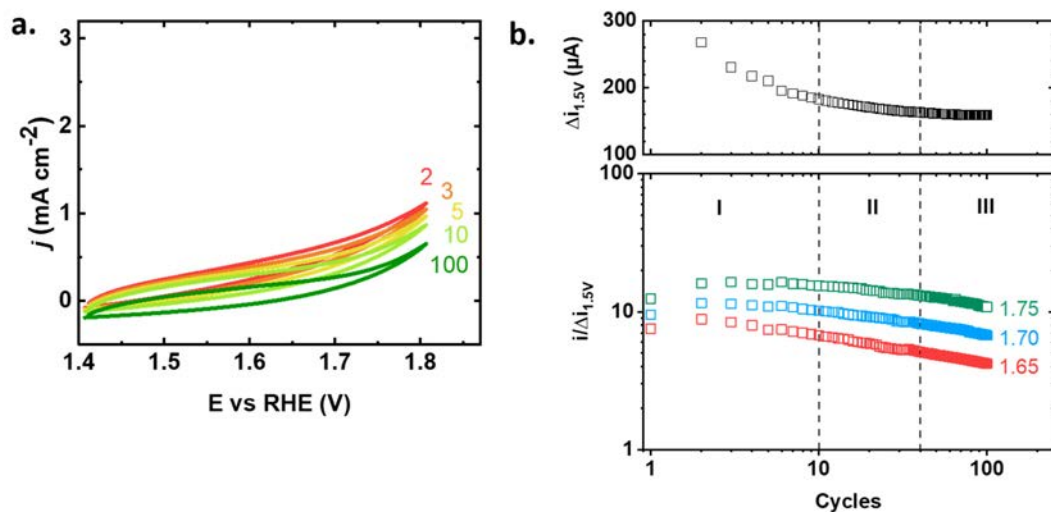


Figure S14. **a.** Series of CV of MnO_x performed at the samples on graphite foil. CV with 100 mV s^{-1} in 0.1 M NaOH . **b.** Average current ratios $i/\Delta i_{1.5V}$ as function of cycles at selected potentials of MnO_x . The data was evaluated during the first 100 cycles (open squares). The dashed lines delimit three different regions, labeled as: I, II and III.

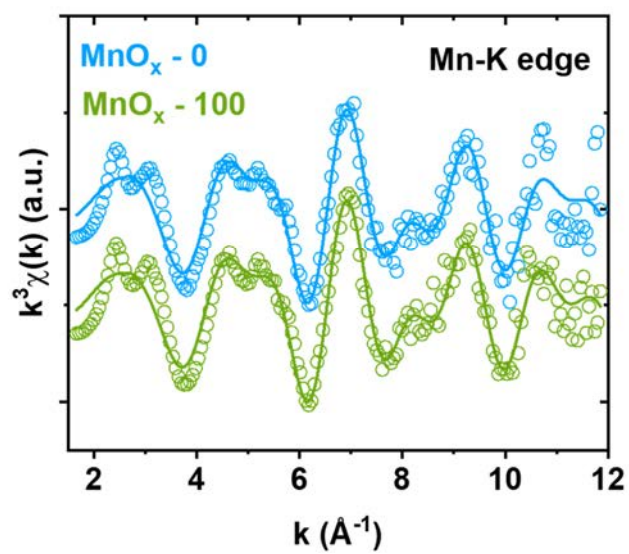


Figure S15. k^3 -weighted EXAFS spectra of pristine MnO_x ($\text{MnO}_x - 0$) and after 100 cycles ($\text{MnO}_x - 100$) recorded at the Mn-K edge. The solid lines represent the respective EXAFS simulations. The symbols represent the measurement.

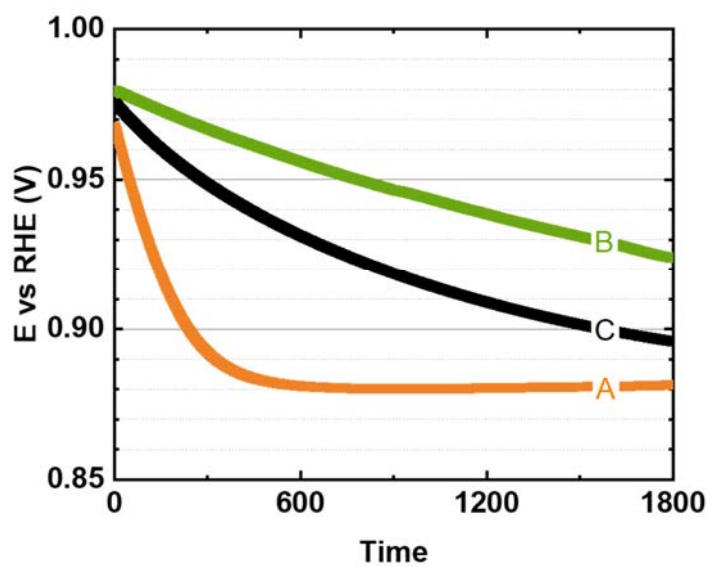


Figure S16. Open-circuit voltage profile during 30 minutes after 100 cycles of catalysis for three samples of MnO_x .